ACS OMEGA

http://pubs.acs.org/journal/acsodf

Article

Preparation of a New Biocomposite Designed for Cartilage Grafting with Antibiofilm Activity

Sara Targonska, Justyna Rewak-Soroczynska, Agata Piecuch, Emil Paluch, Damian Szymanski, and Rafal J. Wiglusz*

Cite This: *ACS Omega* 2020, 5, 24546−24557

Read Online

ACCESS | Metrics & More | Article Recommendations | Supporting Information

ABSTRACT: New polymer−inorganic composites with antibiofilm features based on the granulated poly(tetrafluoroethylene) (PTFE) and apatite materials were obtained using a standard hydraulic press. The study was performed in hydroxy- and fluorapatites doped with different amounts of silver ions and followed by heat treatment at 600 °C. The structural, morphological, and physicochemical properties were determined by X-ray powder diffraction (XRD), Fourier transform infrared (FT-IR) spectroscopy, scanning electron microscopy-energy-dispersive spectrometry (SEM-EDS), and transition electron microscopy (TEM). The antibacterial properties of the obtained materials were evaluated against Gram-negative pathogens such as *Pseudomonas aeruginosa*, *Klebsiella pneumoniae*, and *Escherichia coli* as well as against Gram-positive bacteria *Staphylococcus epidermidis*. The cytotoxicity assessment was carried out on the red blood cells (RBC) as a cell model for in vitro study. Moreover, the biofilm formation on the biocomposite surface was studied using confocal laser scanning microscopy (CLSM).

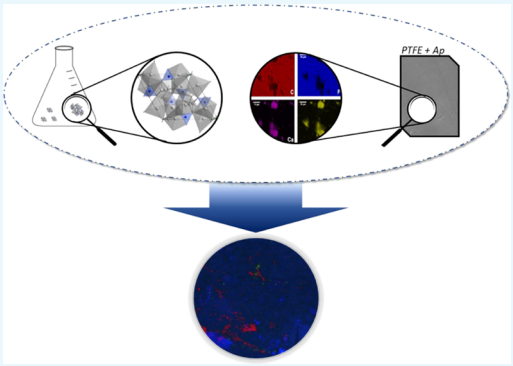

1. INTRODUCTION

Hydroxyapatite ($Ca_{10}(PO_4)_6(OH)_2$—herein, HAp) is well known as a major inorganic component of teeth and bones occurring naturally in human body and is characterized by high biocompatibility and low cytotoxicity to eukaryotic cells. Silver, gold, copper, and zinc metals are well known due to their antimicrobial properties and could be easily used as dopant in apatite-based materials. The hexagonal structure of apatite belongs to the $P6_3/m$ space group and allows the cations to localize in the 4(f) and 6(h) positions and is able to accommodate a variety of univalent as well as divalent and trivalent cations as substituents.[1] The substituted materials can gain new properties due to the presence of so-called biologically active ions. Moreover, such materials could stimulate the bone tissue for regeneration and promote cell proliferation due to their structural similarity to natural appetites. Furthermore, the dopant may prevent bacterial and fungal growth in a graft place.[2−4]

Thus, metal-doped materials can be applied as a promising alternative to the traditional antibiotic therapies.[5] Additionally, apatite-based materials have attracted much attention as drug-delivery systems because of combining several action mechanisms. First, a therapeutic role is fulfilled by apatite-based products used as an implant or bone reconstruction materials. Additionally, dedicated drugs may be applied precisely in a disease spot. More effective treatment with fewer side effects can be obtained by the application of the metal-doped apatite in combination with antibiotics or other drugs. It has been also proved that bacterial resistance to inorganic particles is lower than that to antibiotics due to the different mechanisms of action (MOA).[6,7] It has been reported that metal-ion-doped nanoparticles have shown antimicrobial activity mainly because of free ion release. The presence of free ions can disrupt or destruct the secondary and tertiary structures of proteins (e.g., enzymes or membrane components), leading to the cell dysfunction and increasing membrane permeability. The protein structure disruption could be a result of the thiol group interactions with the Ag^+ ions and the formation of the S−Ag bonds. Metal ions, including the Ag^+ ions, can penetrate cell walls without permanently damaging the membranes or rupturing the cells. Moreover, reactive oxygen species (ROS) are produced in an abnormally large amount (oxidative stress) because of the use of metal-ion-based compounds. Furthermore, metal-ion-based nanoparticles can also be harmful to DNA materials, leading to the inhibition of their replication.[4,8−12] Silver is well known for strong antimicrobial activity against various bacterial and fungal species,[2,13,14] but there are bacteria nonsusceptible to

Received: June 24, 2020
Accepted: August 28, 2020
Published: September 15, 2020

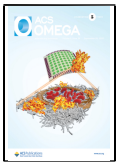

https://dx.doi.org/10.1021/acsomega.0c03044
ACS Omega 2020, 5, 24546−24557

Ag^+-ion-doped HAp, such as *Enteroccocus faecalis*, *Bacillus subtilis*, and *Serratia marcescens*.[15,16]

The apatite-based substances could be used in bone grafting as the implant components. Use of the materials with antimicrobial properties, e.g., silver-doped apatites, could reduce the risk of implant-associated infections after a surgery.[17] Bacterial strains with an ability of biofilm formation can be a major problem because of their high resistance to antimicrobial agents, even 1000-fold higher than planktonic forms. Thus, there is an urgent need for effective antibiofilm substances and materials that prevent bacterial and fungal adhesion.[18−21]

The composite materials are characterized by combining and highlighting the best features of substances that are built by. Since the polymeric industry has been extremely developed, such materials influence all areas of life, including medicine, biochemistry, pharmacy, preparation of drugs, and biologically active substances.[22,23] In the present work, very attractive biocomposites have been designed for cartilage grafting with antibiofilm activities. It has been proved that the obtained materials have great potential in the field of modern nanotechnology and bioapplications focusing on the antibacterial properties. Furthermore, the potential antibacterial properties of novel biocomposites materials were checked and analyzed in detail. The innovation of the proposed biomaterials can be related to the possibility of using them for simultaneous regenerative medicine and in vivo imaging.

2. MATERIALS AND METHODS

2.1. Synthesis of the Silver-Doped Hydroxy- and Fluorapatite (FAp). Calcium hydroxyapatite and fluorapatite (herein FAp) nanopowders were synthesized using the aqueous synthesis route, separately. To obtain silver-doped apatite powders, stoichiometric amounts of $Ca(NO_3)_2{\cdot}4H_2O$ (99.0−103.0%, Alfa Aesar), $NH_4H_2PO_4$ (>99.0%, Acros Organics), $AgNO_3$ (99.8%, POCH), and NH_4F (>98.0%, Alfa Aesar) were used. The concentration of silver dopant was set to 1.0, 2.5, and 5.0 mol % in a ratio of total calcium-ion molar content in the following procedure. All substrates were dissolved in deionized water and mixed in a reaction vessel. The reaction was carried out for 2 h at 100 °C. For pH monitoring, ammonia ($NH_3{\cdot}H_2O$, 25%, POCH) was used and the pH value was maintained at 9.0. After synthesis, all powders were purified with deionized water four times to remove the remaining ammonia ions, dried at 70 °C for 12 h, and heat-treated at 600 °C for 6 h with a temperature increase of 3.5 °C/min. The obtained powders after heat treatment were described as: x mol % Ag^+:$Ca_{10}(PO_4)_6(OH)_2$ and x mol % Ag^+:$Ca_{10}(PO_4)_6F_2$ (where x = 1.0, 2.5, and 5.0) of hydroxyapatite and fluorapatite matrix, respectively. The pellets of pure powders were prepared by a standard laboratory hydraulic press, applying a maximum force of 15 kN on 1.6 g of powder for 60 s. The radius of the obtained pellets was set at 10 mm (see Figure S1a,b).

2.2. Preparation of the Silver-Doped Hydroxy- and Fluorapatite Composites. A dispersion of poly(tetrafluoroethylene) (PTFE) in deionized water (Inbras, Poland) was used to produce polymer−inorganic composites. The PTFE concentration and density were 60 wt % and 1.5 g/cm^3, respectively, as revealed by the manufacturer. The PTFE dispersion has been detected as molecules with spherical shape in a range of 0.1−0.3 μm. In the case of biocomposite preparation, the apatite powders were added to the water dispersion and then sonicated for 2 h. Fluorapatite doped with the highest amount of silver (5 mol % Ag^+) was chosen as a filling material along with hydroxyapatite doped with 2.5 mol % Ag^+ ions (to compare the highest concentration of silver ions in both types of apatite matrix). Then, the mixtures were air-dried. The composites with 1.0, 5.0, and 10.0 wt % of the fillers were formed using a standard hydraulic press under 15 kN force. The radius and weight of obtained pellets were set at 10 mm and 0.04 ± 0.001 g, respectively. The obtained materials are listed in Table 1. The representative pellets of tetrafluoroethylene with 10 wt % of hydroxyapatite (PTFE@Ag^+:10HAp) and 10 wt % of fluorapatite (PTFE@Ag^+:10FAp) composites are shown in Figure S1c,d, respectively.

Table 1. Summary of the Obtained Materials

symbol	PTFE (wt %)	HAp/FAp (wt %)
x mol %Ag:HAp[a]	0	100
x mol %Ag:Fap[a]	0	100
PTFE@Ag^+:1HAp	99	1
PTFE@Ag^+:5HAp	95	5
PTFE@Ag^+:10HAp	90	10
PTFE@Ag^+:1FAp	99	1
PTFE@Ag^+:5FAp	95	5
PTFE@Ag^+:10FAp	90	10

[a]where x = 1.0, 2.5, 5.0.

2.3. Characterization. The development of the crystal phase was checked by X-ray diffraction (XRD) patterns for all nanopowders. The patterns were collected in the 2θ range of 5−120° with an X'Pert PRO X-ray diffractometer (Cu Kα_1, 1.54060 Å) (PANalytical). The XRD patterns were assigned using the Joint Committee on Powder Diffraction Standards Database (JCPDS) and Inorganic Crystal Structure Database (ICSD) and then analyzed. The morphology and the chemical composition were checked by an FEI Nova NanoSEM 230 scanning electron microscope equipped with energy-dispersive spectrometer (EDAX Genesis XM4). Scanning electron microscopy (SEM) images and EDS spectra/maps were recorded at 5.0 and 20.0 kV, respectively. After drying by an infrared lamp, the sample was put under the microscope. The microstructure of the nanopowders was measured by an FEI Titan high-resolution transmission electron microscope (HRTEM) operating at 180 kV.

Fourier transform infrared (FT-IR) spectra were recorded using a Thermo Scientific Nicolet iS50 FT-IR spectrometer equipped with an Automated Beam splitter exchange system (iS50 ABX containing DLaTGSKBr detector), built-in all-reflective diamond ATR module (iS50 ATR), Thermo Scientific Polaris, and He−Ne laser as an IR radiation source. Infrared spectra were measured in the 4000−500 cm^{-1} range in KBr pellets with a spectral resolution of 4 cm^{-1} at room temperature.

Absorption spectra were determined using an Agilent Cary 5000 spectrophotometer, employing a spectral bandwidth (SBW) with a spectral resolution of 0.1 nm in the visible and ultraviolet range and recorded in the 240−1500 nm range at room temperature.

The hydrodynamic size of the poly(tetrafluoroethylene) (PTFE) particles dispersed was measured using the dynamic light scattering technique supported by Zetasizer Nano-ZS (Malvern) that is equipped with a He−Ne 633 nm laser.

https://dx.doi.org/10.1021/acsomega.0c03044
ACS Omega 2020, 5, 24546−24557

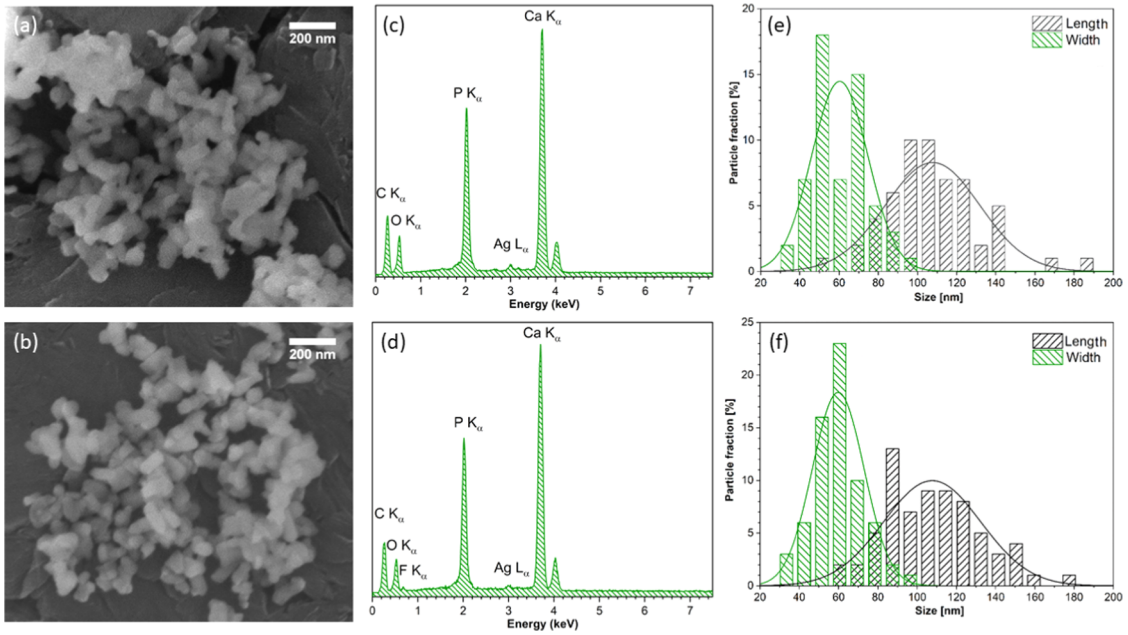

Figure 1. SEM images (a, b), EDS spectra (c, d), and size distribution (e, f) of 2.5 mol % Ag^+:HAp (top) and 5.0 mol % Ag^+:FAp (bottom) powders heat-treated at 600 °C.

The concentration of the released silver ions was checked using atomic absorption spectroscopy (AAS) with an atomic absorption spectrometer iCE 3300 (Thermo Scientific Instrument) with the wavelength set at 328.1 nm.

2.4. Ion Release. The release of silver ions was investigated for tetrafluoroethylene with 10 wt % hydroxyapatite (PTFE@Ag^+:10HAp) and 10 wt % fluorapatite (PTFE@Ag^+:10FAp) composites. The composite pellets with predetermined weights were placed in the Luria–Bertani (LB) broth (LENNOX) (Oxoid) and stirred for 1, 6, 12, and 24 h. Then, the silver-ion concentration was measured by the AAS technique. The ion release in the LB medium was important for further antibiofilm activity testing because this broth was used to perform a test.

2.5. Antibacterial Activity. The antibacterial activity of fluor- and hydroxyapatites doped with Ag^+ ions (1.0, 2.5, and 5.0 mol %) was tested using the following strains: *Escherichia coli* ATCC 35218, *Klebsiella pneumoniae* ATCC 700603, *Pseudomonas aeruginosa* ATCC 27853, and *Staphylococcus epidermidis* ATCC 12228. All strains came from the collection of the Institute of Genetics and Microbiology, University of Wroclaw. The strains were cultivated overnight at 37 °C in the LB (LENNOX) (Oxoid) medium, centrifuged, and suspended in saline (0.9% NaCl) to obtain an optical density of 0.5 McFarland. Suspensions were then diluted 10× with 10 μL of cell suspension and transferred to a 96-well polystyrene plate. The colloidal solutions of hydroxy- and fluorapatites doped with the above-mentioned dopants of Ag^+ were diluted in the saline to obtained the final concentrations of 10, 25, 50, and 100 μg/mL. Then, the solutions (200 μL) were added to wells with bacterial suspensions and plates and incubated for 2 h. Further, the bacterial suspensions were diluted in saline and 10 μL of the bacterial solution from each dilution was spotted on a Muller–Hinton agar plate for CFU/mL determination. The plates were incubated at 37 °C for 24 h. The incubated bacterial cells in saline solution were used as the control. Additionally, undoped apatites were tested for antibacterial activity.

Antibiofilm activity was evaluated for two groups of samples: hydroxy- and fluorapatites doped with 1.0, 2.5, and 5.0 mol % of Ag^+ in the form of pellets. Additionally, the materials with the highest dopant concentration (2.5 and 5.0 mol % Ag^+) were mixed with poly(tetrafluoroethylene) (PTFE). The pure PTFE sample in the form of foil (10 mg pieces) was used as the control for the second group. All pellets were incubated at 37 °C overnight with 1 mL of *P. aeruginosa* ATCC 27853 solution in LB medium (OD = 0.1) with shaking (125 rpm). Then, the absorbance (λ = 550 nm) of bacterial solution was measured using a microplate reader (Varioskan LUX). Further, the obtained results were compared with the absorbance of growth control sample and the percentage was calculated. The pellets were rinsed with saline and dyed for 30 min using a fluorescent dye (laser line λ_{exc} = 488 nm) and propidium iodide (laser line λ_{exc} = 543 nm) (both at the concentration of 1 μL/mL). Then, the pellets were rinsed and observed using confocal microscopy (Olympus IX83 Fluoview FV 1200, camera CCD Hamatsu C13440, magnification 40×). Additionally, the continuum laser with λ_{exc} = 405 nm was used to observe the surface of the apatites.

2.6. Hemolysis. A hemolysis test was performed according to the standard protocol with a slight modification.[24] Hemolysis was conducted using ram erythrocytes (ProAnimali) diluted to 1:1 in phosphate-buffered saline (PBS). Concentrated colloidal nanomaterial suspensions were added to blood samples to obtain the final concentrations of 50 and 100 μg/mL. Sodium dodecyl sulfate (SDS) solution (1%) and PBS were used as positive (100% of hemolysis) and negative controls, respectively. All samples were incubated at 37 °C for 1.5 h and centrifuged. Then, the absorbance of the supernatant at λ = 540 nm was measured with a plate reader (Varioskan LUX). The obtained measurements were compared to the absorbance of the positive control (the percentage of hemolysis was calculated using the formula below), and the statistical analysis was performed using one-way analysis of variance (ANOVA) test ($p < 0.05$).

https://dx.doi.org/10.1021/acsomega.0c03044
ACS Omega 2020, 5, 24546−24557

$$\text{hemolysis} = \frac{\text{sample absorbance} - \text{negative control absorbance}}{\text{positive control absorbance} - \text{negative control absorbance}} \times 100$$

3. RESULTS AND DISCUSSION

3.1. Surface Morphology. Scanning electron microscopy (SEM) as well as transmission electron microscopy (TEM) were used to study the morphological properties of the heat-treated hydroxy- and fluorapatites doped with Ag^+ ions. Figure 1a,b shows the representative SEM images of the 2.5 mol % Ag^+-ion-doped hydroxyapatite and 5.0 mol % Ag^+-ion-doped fluorapatite, respectively. It has been demonstrated that the particles possess an elongated shape with length in the range of 50−150 nm and width in the range of 30−100 nm. The histogram of particle size distribution is shown in Figure 1e,f. The powders do not appear to be agglomerated in comparison to our previous works.[25,26] Nanometric powders preclude to get a higher-resolution image with the help of the SEM technique; therefore, the surface morphology cannot be characterized in detail. Moreover, the EDS spectra were recorded for the samples and are presented in Figure 1c,d. It has been confirmed that the Ag^+ and F^- ions are doped to obtain the desired structures. The Ca/P ratios have been estimated to be around 1.67, which is quite close to the theoretical ratio. In the case of the investigated materials, the calcium ion was partially replaced by the silver ion. The substitution effect of dopant ions was examined as well as confirmed for both hydroxyapatite and fluoride-substituted hydroxyapatite.[27] The amounts of chemical elements calculated from the EDS spectra are presented in Table 2.

Table 2. Element Analysis of the Investigated Powders Based on the EDS Techniques

sample	Ag^+ (mol %)[a,b]	Ca/P (mol/mol)[c]	F^- (mol)[a,d]
5.0 mol % Ag^+:HAp	4.4	1.6	
2.5 mol % Ag^+:HAp	2.5	1.6	
1.0 mol % Ag^+:HAp	1.3	1.6	
5.0 mol % Ag^+:FAp	1.2	1.6	1.6
2.5 mol % Ag^+:FAp	0.6	1.7	1.7
1.0 mol % Ag^+:FAp	0.5	1.7	1.6

[a]The relative error of the EDS method is ranging between 10.0 and 20.0% for minor elements.[28] [b]Calculated from the equations where $n_{Ag^+} = 10 \times n_{Ag^+}/(n_{Ca^{2+}} + n_{Ag^+})$. [c]Calculated from the equations where $n_{Ca^{2+}}/n_{P^{5-}} = (n_{Ca^{2+}} + n_{Ag^+})/n_{P^{5-}}$. [d]Calculated from the equations where $n_{F^-} = 2 \times n_{F^-}/4.8\%$.

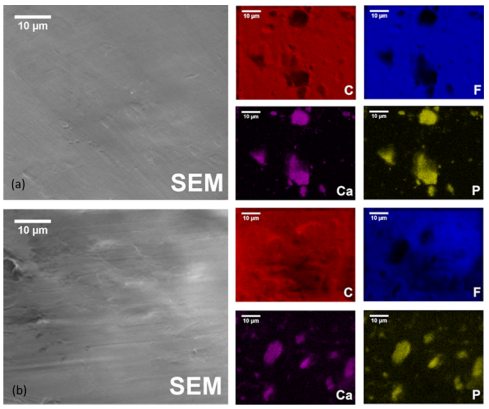

Figure 3. SEM images and EDS elemental mapping of (a) PTFE@Ag^+:10HAp and (b) PTFE@Ag^+:10FAp.

The shape and size of the obtained powders were determined by TEM images. The representative images of 5.0 mol % Ag^+:HAp nanopowder are shown in Figure 2. The TEM images confirm that the obtained materials (heat-treated at 600 °C) are nanosized with dimensions increasing from about 60 nm to 120 and 180 nm width and length, respectively. The heat-treated materials tend to agglomerate. The HRTEM image (see Figure 2b) presents the typical ordering of hexagonal structure. Intracolumn and intercolumn ordering is the result of the specific position of OH^- groups. In the hexagonal HAp crystal structure, the OH^- groups are arranged in twofold disorder columns, directed from the mirror planes and passing through the closer-coordinating calcium ion.[29]

To obtain distribution of the elements in the PTFE@Ag^+:10HAp and PTFE@Ag^+:10FAp samples, energy-dispersive X-ray spectroscopy (EDS) measurements were performed. The obtained EDS elemental mapping is shown in Figure 3a,b. It has been found that PTFE samples have been uniformed for the distribution of the F and C elements, except for the locations where the Ca and P elements have been highly accumulated. The distribution of the aggregated composition

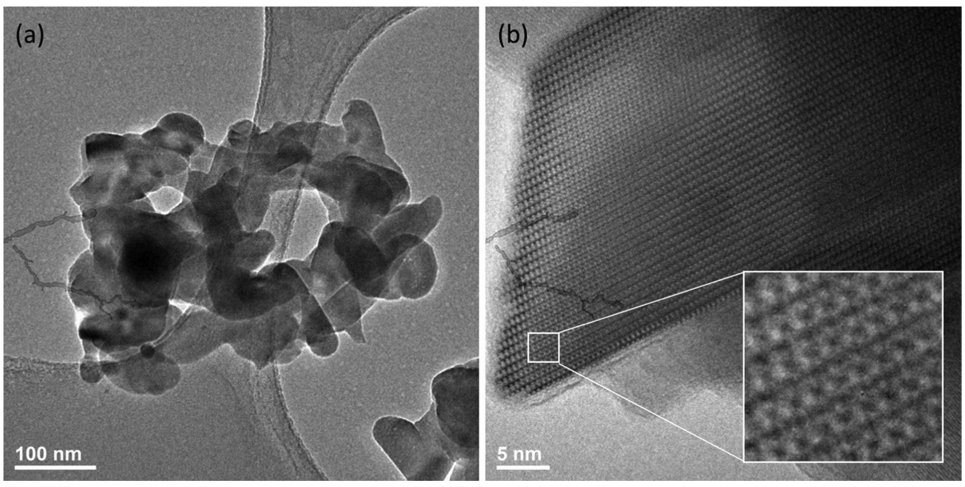

Figure 2. TEM image (a) and HRTEM image (b) of 5.0 mol % Ag^+:HAp powders heat-treated at 600 °C.

https://dx.doi.org/10.1021/acsomega.0c03044
ACS Omega 2020, 5, 24546−24557

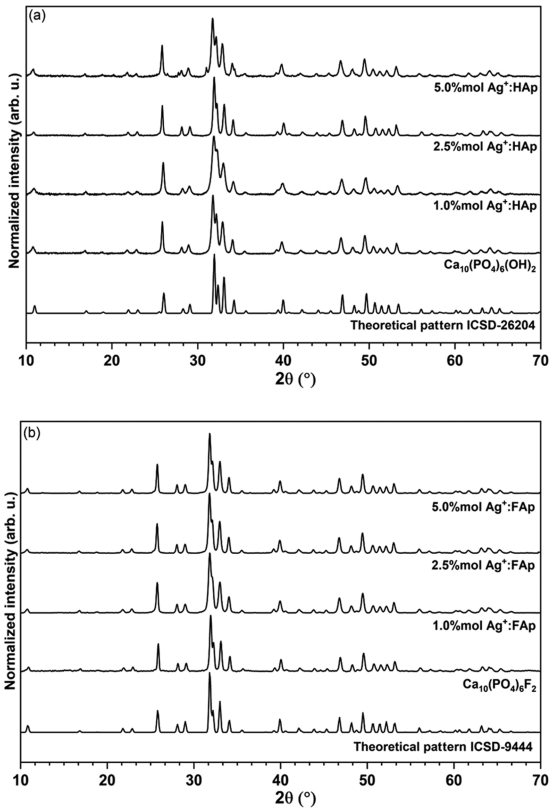

Figure 4. X-ray diffraction patterns of hydroxyapatite (a) and fluorapatite (b) of undoped and silver dopant samples.

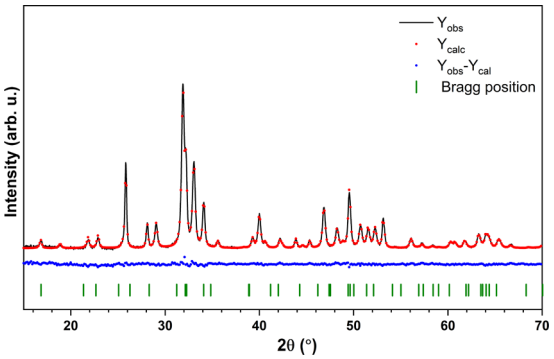

Figure 5. Representative result of the Rietveld refinement of $Ca_{9.9}Ag_{0.1}(PO_4)_6F_2$.

of those elements has indicated that HAp and FAp have been randomly distributed in the poly(tetrafluoroethylene) samples.

3.2. Structural and Morphological Characterization.

The structural properties of nanopowders heat-treated at 600 °C were determined using the XRD technique. The X-ray powder diffraction patterns of x mol % Ag^+:HAp and x mol % Ag^+:FAp (where x = 0.0, 2.5, and 5.0) were compared to the theoretical pattern of hydroxyapatite (ICSD-26204)[30] and fluorapatite (ICSD-9444)[31] and are shown in Figure 4. It can be noted that all diffraction peaks of the obtained samples corresponded very well with the positions of the peaks ascribed to the reference standards of the apatite phase (space group $P6_3/m$). No other phases have been detected. The most intense peaks of the hydroxyapatite structure have been observed at 25.8° (003), 31.8° (211), 32.2°, 32.8°, and 34.1°, and those of fluorapatite at 25.9° (002), 31.9° (211), 32.2° (112), 33.1° (300), and 34.1° (202). The crystallographic planes of the obtained nanoparticles are shown in brackets.

In the apatite host lattice, two calcium positions (Ca(1) and Ca(2)) with C_3 and C_s symmetries are to be substituted.[32,33] In hydroxy- and fluorapatite matrix, the calcium ions at the Ca(1) sites are coordinated by nine oxygen atoms derived from PO_4^{3-} groups. The Ca(2) site with C_s symmetry is surrounded in hydroxyapatite by six oxygen atoms from PO_4^{3-} and one hydroxyl group constructed irregular polyhedron with the formula CaO_6OH. In the case of the fluorapatite matrix, the hydroxyl group is replaced by a fluoride ion. The unit cells of calcium hydroxyl and fluorapatites are doped with silver ions as well as the coordination polyhedra of Ca^{2+} cations in both sides (see Figure S2). The similarity of the effective ionic radius of silver ions (CN_7—1.22 Å) to calcium ions (CN_9—1.18 Å, CN_7—1.06 Å) gives a possibility to substitute calcium ions with silver ions.[30,34]

The structural refinement was calculated using a Maud program version 2.93[35,36] based on the apatite hexagonal crystal structure with better approximation and indexing of the Crystallographic Information File (CIF). The quality of the structural refinement was checked by R-values (R_w, R_{wnb}, R_{all}, R_{nb}, and σ), which were applied to obtain a structural refinement with better quality and reliability. The hexagonal-phase formation as well as the successful incorporation of Ag^+ ions into the hydroxyapatite were confirmed. Figure 5 presents the representative Rietveld pattern for the 1.0 mol % Ag^+:FAp sample.

Moreover, hydroxyapatite and fluorapatite samples crystallized in the hexagonal lattice structure. The sixfold inclination of the c-axis at 120° to three a-axes is seen in the crystal system. In the fluorapatite, the hydroxyl groups have been substituted by smaller fluoride ions, showing the reduction of the a-axis dimension without a change in the c-axis length. Even small differences in effective ion radius can influence

Table 3. Unit Cell Parameters (a, c), Cell Volume (V), Grain Size, and Refine Factor (R_w) of $Ca_5(PO_4)_3OH$ and $Ca_5(PO_4)_3F$ Doped with x mol % Ag^+ Powder

sample	a (Å)	c (Å)	V (Å^3)	size (nm)	R_w (%)
single-crystal $Ca_5(PO_4)_3OH$	9.424(4)	6.879(4)	529.09(44)		
1.0 mol % Ag^+	9.4359(2)	6.888(8)	531.19(66)	34.6(1)	2.5
2.5 mol % Ag^+	9.4321(2)	6.886(9)	530.61(48)	42.9(1)	2.6
5.0 mol % Ag^+	9.3831(3)	6.892(5)	525.53(65)	69.2(2)	2.7
single-crystal $Ca_5(PO_4)_3F$	9.3672(1)	6.8844(1)	523.15(1)		
1.0 mol % Ag^+	9.3772(2)	6.8891(5)	524.61(9)	56.9(2)	2.8
2.5 mol % Ag^+	9.3828(1)	6.8921(0)	525.47(0)	68.1(3)	2.6
5.0 mol % Ag^+	9.3786(9)	6.8896(4)	524.82(2)	74.4(8)	2.5

https://dx.doi.org/10.1021/acsomega.0c03044
ACS Omega 2020, 5, 24546−24557

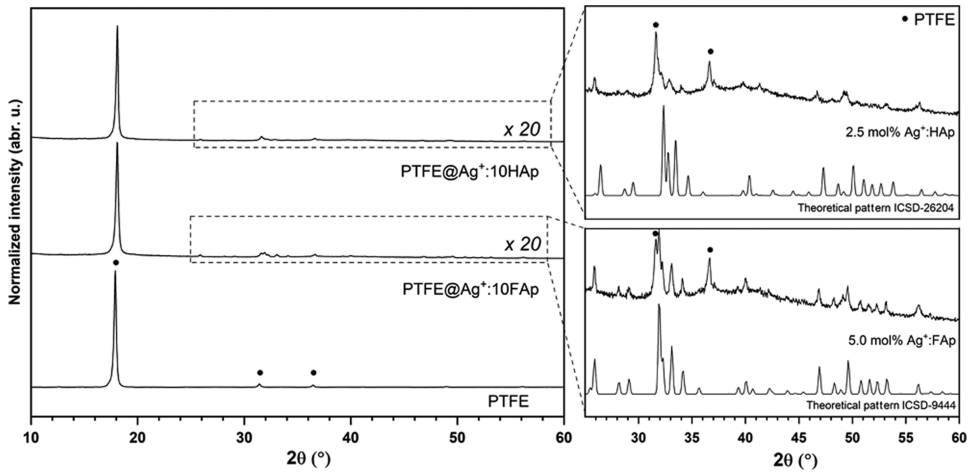

Figure 6. X-ray diffraction pattern of pure tetrafluoroethylene and composites with 10 wt % hydroxyapatite and 10 wt % fluorapatite.

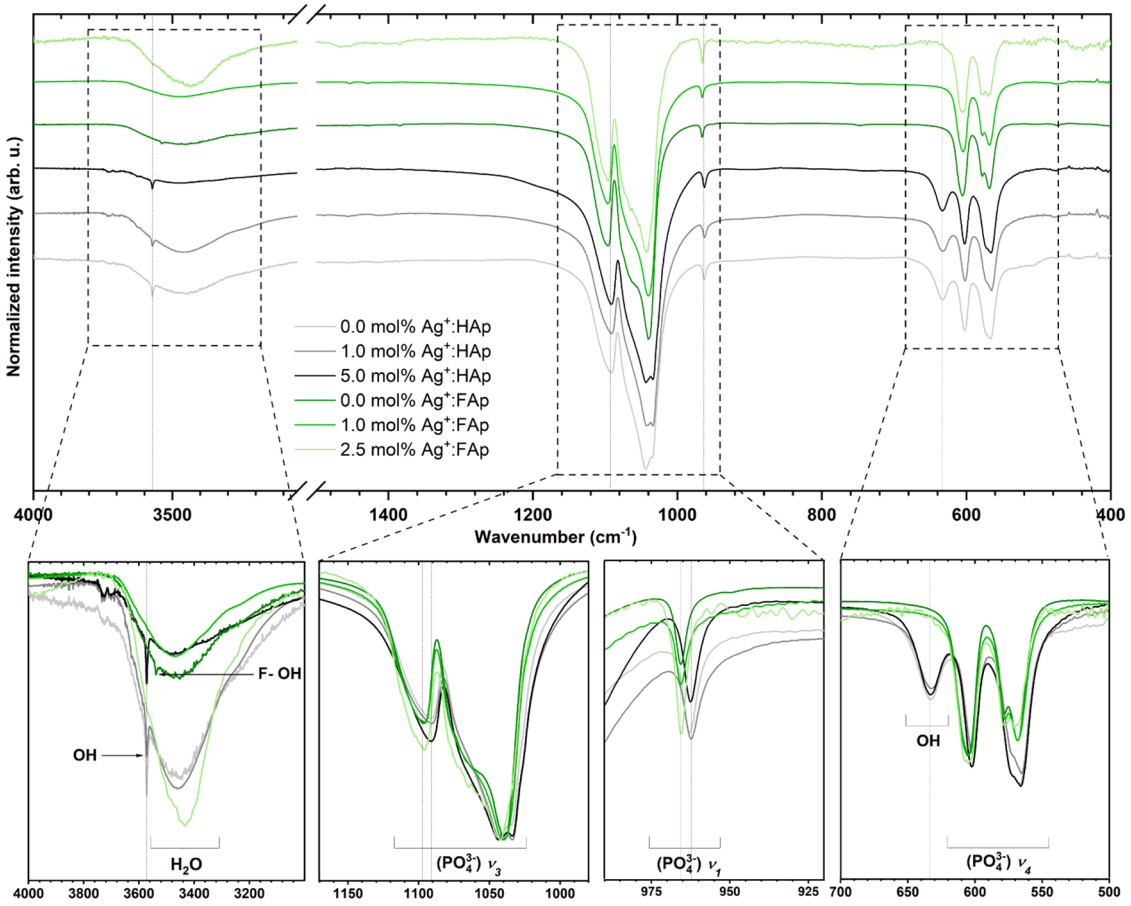

Figure 7. FT-IR spectra of the doped and undoped hydroxyapatites and fluorapatites.

lattice parameters. The calculated unit cell parameters (a, c), cell volume (V), grain size, and refine factor (R_w) of hydroxyapatite and fluorapatite are presented in Table 3. As has been expected, the dimensions of the a-axis and cell volume were smaller in the case of fluorapatite than the hydroxyapatite lattice.

Furthermore, it has been observed that the fluorapatite turned into a single-phase hydroxy fluorapatite during the heat treatment process (see Figure S3). Therefore, it can be suggested in accordance with the chemical formula of the obtained materials and EDS analysis (see Table 2) that, in the fluorapatite structure, the hydroxyl groups coexist with fluoride ions.[37]

The X-ray patterns of the PTFE@Ag^+:10HAp and PTFE@Ag^+:10FAp composites are shown in Figure 6. The most intense peaks at 18.0° have been attributed to PTFE, as well as weak peaks at 31.4 and at 36.4°.[38,39] In the range of 20−60°, the spectra were multiplied 20 times to present the lines corresponding to the apatite matrix.

The particle size distribution was estimated by laser diffraction, assuming that the molecules are spherical (see Figure S4). The measurement was repeated five times, and the

https://dx.doi.org/10.1021/acsomega.0c03044
ACS Omega 2020, 5, 24546−24557

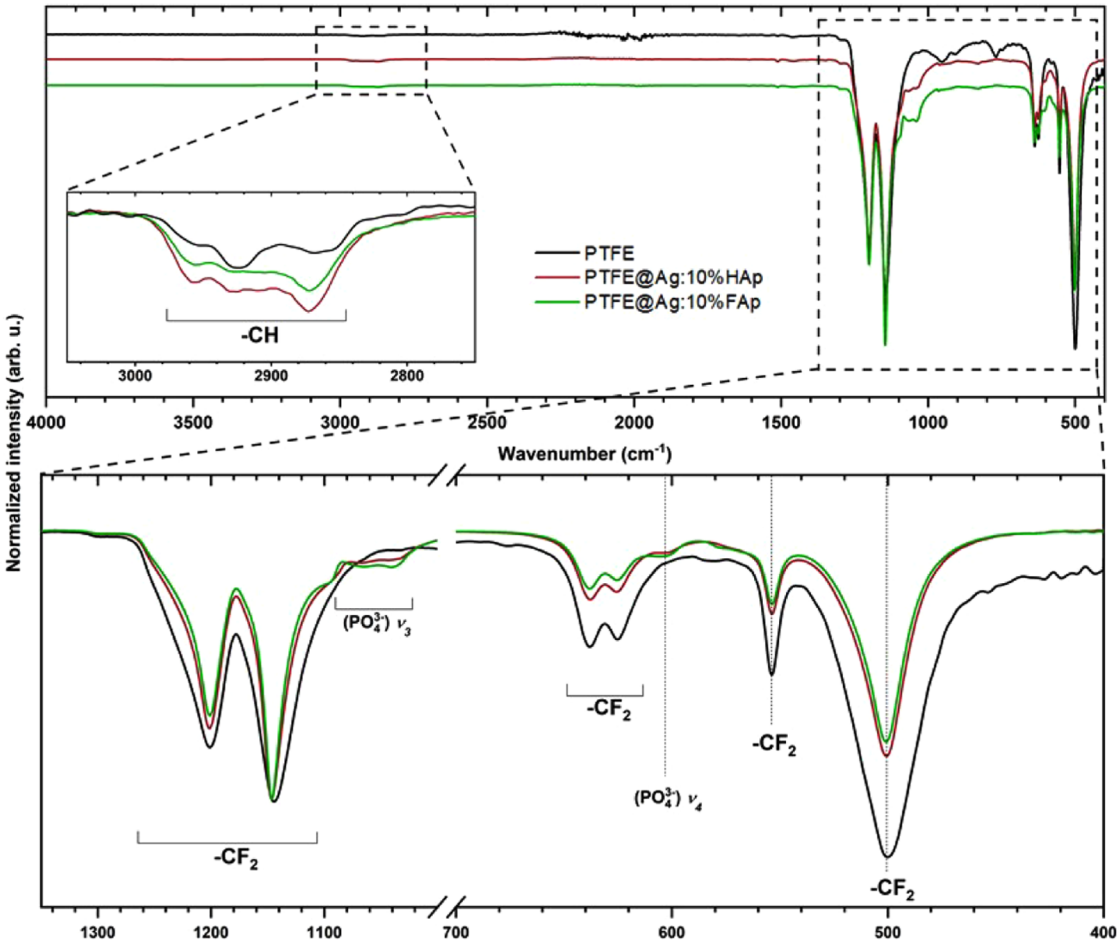

Figure 8. FT-IR spectra of pure tetrafluoroethylene and the composites with 10 wt % of hydroxyapatite and 10 wt % of fluorapatite.

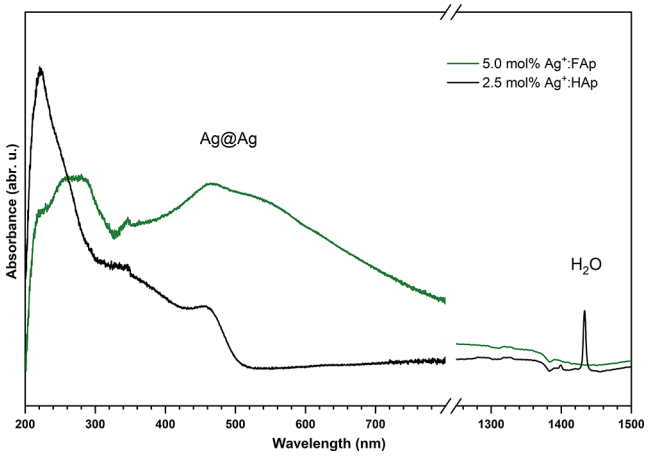

Figure 9. Absorption spectra of the doped hydroxyapatites and fluorapatites recorded at 300 K.

average particle size is equal to 160.4 nm. The radius of all molecules is in the range of 70−300 nm according to the distributor information.

3.3. Infrared Spectra. Identification of the functional groups present in the prepared powders was conducted using infrared spectroscopy. The presence of peaks related to phosphate and hydroxyl groups was confirmed (see Figure 7) and described based on previous papers.[40−42] The spectrum of the fluorapatite sample displays a systematic shifting of peak position about the hydroxyapatite matrix. The most intense peaks associated with the $\nu_3(PO_4^{3-})$ triply degenerated antisymmetric stretching mode of phosphate groups were located at 1033 and 1090 cm^{-1} of hydroxyapatite and at 1043 and 1099 cm^{-1} of fluorapatite. The nondegenerate symmetric stretching bands $\nu_1(PO_4^{3-})$ were observed at 962 and 966 cm^{-1} of hydroxyapatite and fluorapatite, respectively. Frequency shifts of the PO_4^{3-} modes can be related to the smaller cell volume of fluorapatite than hydroxyapatite (see Table 2) in accordance with Balan et al.,[42] whereas the $\nu_4(PO_4^{3-})$ triply degenerated vibrations were detected at 603 and 565 cm^{-1}. In the case of hydroxyapatite, the narrow peaks at 3751 and 634 cm^{-1} were matched to the stretching and bending vibrations of OH^- modes, confirming the presence of hydroxyl groups in the crystal structure. As it has been reported,[27,43] the band at 3540 cm^{-1} appeared in the infrared spectra when more than 30 mol % of the F^- ions were incorporated into the apatite matrix, which means that more than 30% of OH^- groups are replaced by fluoro ions.[37,44] Moreover, the peak at 3538 cm^{-1} for undoped fluorapatite matrix has been assigned to F−OH^- vibrations.

The FT-IR spectra of pure tetrafluoroethylene (PTFE) as well as the composite materials, PTFE@Ag^+:HAp and PTFE@Ag^+:FAp, are presented in Figure 8. The weak peaks located at 2873 and 2930 cm^{-1} were matched with the stretching vibrations of −CH bonds. The peaks at 1145 and 1201 cm^{-1} were ascribed to the $-CF_2$ groups, asymmetric and symmetric stretching modes, respectively. The peaks located in the lower-

https://dx.doi.org/10.1021/acsomega.0c03044
ACS Omega 2020, 5, 24546−24557

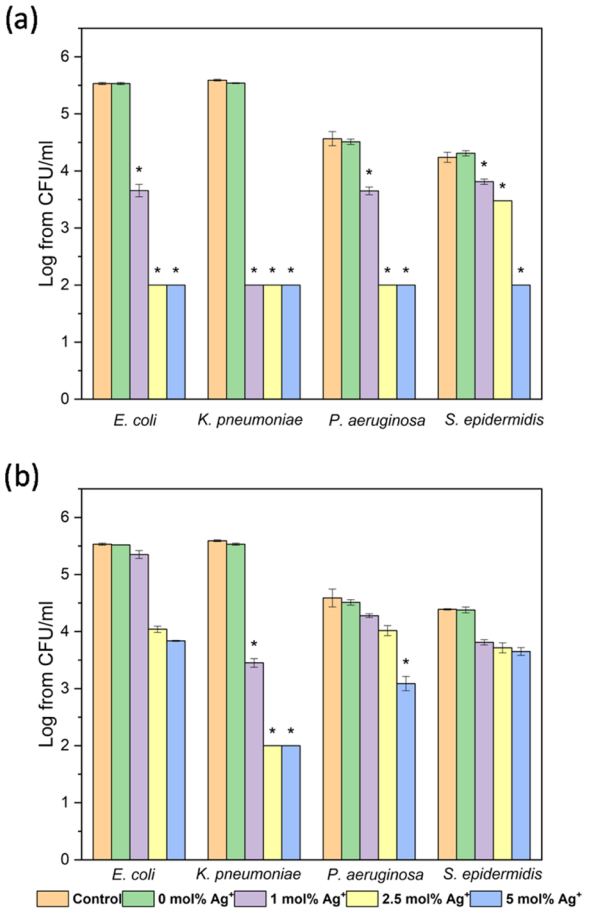

Figure 10. Antibacterial activity of (a) hydroxyapatite and (b) fluoroapatite doped with Ag^+ (1, 2.5, and 5 mol %) at the concentration of 25 μg/mL, against bacterial strains: *E. coli* ATCC 35218, *K. pneumoniae* ATCC 700603, *P. aeruginosa* ATCC 27853, and *S. epidermidis* ATCC 12228; mean ± standard deviation (SD), n = 3; * statistically different from the control.

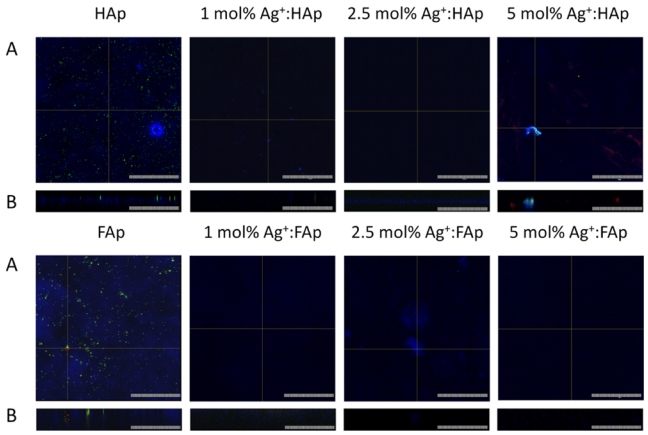

Figure 11. Bacterial biofilm on the surface of hydroxyapatite and fluorapatite doped with 1, 2.5, and 5 mol % Ag^+ pellets: (A) surface and (B) profile (scale bar = 100 μm).

frequency region corresponding to the vibrations of $-CF_2$ groups at 501, 554, and 639 cm^{-1} were matched to the wagging, deformation, and rocking modes, respectively.[45,46] Additionally, the characteristic peaks of the apatite were observed at 1050 and 605 cm^{-1}.

3.4. Absorption. The UV−vis absorption spectra of the obtained materials are shown in Figure 9. The spectra showed characteristic bands related to nanosilver plasmons (Ag-NPs) at 460 nm because of reduction of the Ag^+ ions to silver (Ag^0). The intensity of the absorption peaks suggested that the reduction was more effective for fluorapatite than the hydroxyapatite matrix.

3.5. Ion Release. Time-dependent silver-ion release has been shown in Figure S5. It can be noted that a similar amount of silver ions was released by the hydroxyapatite and fluorapatite PTFE composites. However, it was difficult to explain the significant change of the value after 6 h for the PTFE@Ag^+:10FAp composite, and therefore this point was rejected. In the first hour of the experiment, 1.36 mg of Ag^+ ions for hydroxyapatite and 0.76 mg of Ag^+ ions for fluorapatite were released. Moreover, after 12 h, the concentration of silver ions in both solutions was equal. The silver ions were constantly released up to 24 h, at a rate of about 0.3 mg of Ag^+ ions per hour. These parameters were important for further analysis regarding microbiological activity.

3.6. Species-Dependent Antibacterial Activity. Silver has well-documented antibacterial activity. However, the bactericidal properties of silver-doped apatites are still tested to find the best structure.[47] Thus, the antibacterial activity of fluor- and hydroxyapatites doped with Ag^+ (1.0, 2.5, and 5.0 mol%) was investigated using bacterial strains commonly applied for drug susceptibility testing.

The comparison of fluoro- and hydroxyapatites showed the much higher antibacterial activity of the latter ($p < 0.05$). Hydroxyapatites presented excellent activity against tested strains already when 2.5 mol % Ag^+ doping was applied and at the colloid concentration of 25 μg/mL (Figure 10; in the case of *K. pneumoniae* already at 10 μg/mL—data not shown). However, results obtained for HAp and FAp should not be compared in this study because of the inequality of actual Ag^+ dopants in tested samples. The increase of the concentration up to 50 and 100 μg/mL appeared to be lethal for all of the tested strains (data not shown). Fluorapatites doped with 2.5 mol % Ag^+, on the other hand, at the colloid concentration of 25 μg/mL exhibited much weaker antimicrobial activity (Figure 10, $p < 0.05$). Although lower concentrations were lethal to *K. pneumoniae*, at least 50 μg/mL of the colloids (2.5 and 5 mol % Ag^+) had to be applied to kill the remaining strains (data not shown).

The tolerance level of tested apatites varied among bacterial strains. The most resistant (especially to fluorapatites) was Gram-positive *S. epidermidis*, and the most susceptible was *K. pneumoniae* (Figure 10, $p < 0.05$). The higher viability in comparison to Gram-negative strains might be connected to the structure of the cell surface. Cell penetration by silver ions might be limited due to the thick murein cell wall surrounding the cell. Additionally, the negative charge of peptidoglycan may trap silver ions on the cell surface.[48] The results also showed good antibacterial activity against *P. aeruginosa* and *E. coli*, which is consistent with the previous findings.[47,49]

3.7. Antibiofilm Activity. Antibiofilm activity may be described in two ways: as a prevention of biofilm formation and the ability to eradicate already formed biofilm. Since the possible application of apatite is as grafting material, the present study focused on a biofilm prevention. Confocal microscopy is a useful tool in biofilm structure analysis due to the possibility to scan deeply through specific layers and observe the structure as a three-dimensional (3D) picture.

https://dx.doi.org/10.1021/acsomega.0c03044
ACS Omega 2020, 5, 24546−24557

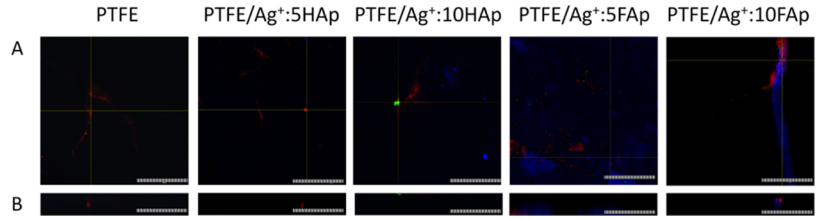

Figure 12. Bacterial biofilm on the surface of PTFE mixed with hydroxy-/fluorapatites with different dopant concentrations of 5 and 10% Ag^+ pellets: (A) surface and (B) profile (scale bar = 100 μm).

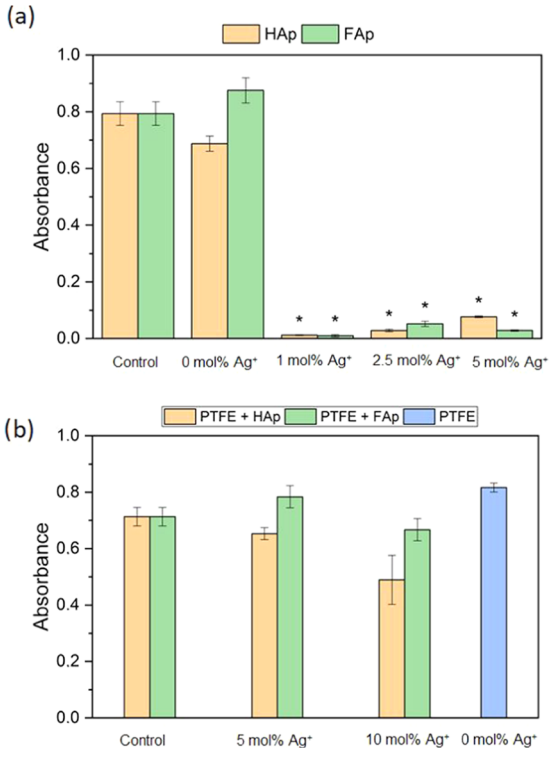

Figure 13. Influence of tablets on *P. aeruginosa* growth compared with the control sample: (a) Ag^+-doped HAp/Fap; (b) Ag^+-doped HAp/FAp mixed with PTFE (mean ± SD, n = 3; * statistically different from the control ($p < 0.05$).

Moreover, confocal microscopy revealed that bacterial biofilm is only slightly formed on the surface of pellets. However, viable cells (green fluorescence) were observed on the surface of undoped hydroxy- and fluorapatites. Virtually no cells were found on the apatites doped with Ag^+ (Figure 11). The antibiofilm activity of these materials was confirmed with bacterial solution absorbance measurement (Figure 13). The results obtained for pure HAp (A = 0.86) and FAp (A = 1.1) were similar to that of the control (A = 1.0), and the bacterial reduction was very high for each of the tested Ag^+-doped compounds. The photographs of the PTFE-apatite composites did not show any bacterial cells (Figure 12). The analysis of absorbance measurements (Figure 13) revealed that the addition of PTFE reduced the antibacterial activity of Ag^+-doped materials. The growth reduction for HAp (5 and 10 mol % of Ag^+) and for FAp-based apatites was not significant (even weak stimulation of growth was detected for FAp doped with 2.5 mol % Ag^+) so the antibiofilm activity observed in confocal microscopy might be a result of an antiadhesive hydrophobic surface of PTFE-based pallets instead of ion release. The pure PTFE sample did not cause any growth reduction, but dead adherent cells were observed (Figure 12).

The antibiofilm activity of Ag^+-doped HAp composites was also confirmed previously by other researchers using common oral pathogens: *Streptococcus mutans*, *Streptococcus sanguinis*, and *Lactobacillus acidophilus*. The strongest activity was observed for 5.0 and 10.0 % dopants, and 1.0 % was not very effective.[50] Such activity against *S. sanguinis* was also confirmed by Besinis et al., who tested bacterial adhesion to the surface of titanium alloy implants coated with silver-doped HAp composites.[51] A weak adhesion was also observed by Zhao and Ashraf on the surface of silver-doped materials.[52] They also detected many bacterial cells on the surface of pure HAp material, which was very similar to the results obtained in present work.[52] Silver-doped composites in a form of microbeads, as well as polymeric poly(methyl methacrylate) (PMMA) materials, were also reported to have an ability to prevent the formation and eradicate preformed bacterial biofilms (*S. aureus* and *P. aeruginosa*).[53,54]

3.8. Hemolytic Activity. Hemolysis assay is one of the tests performed in vitro to check the safety of the chemical compounds. It is necessary to evaluate the hemolytic potential of new substances with the possible application in direct contact with human tissues to eliminate potentially harmful ones. None of the tested compounds was hemolytic above the acceptable level of 5% ($p < 0.05$), which indicates that all of them could be regarded as nonharmful (Figure S6).[55] Nevertheless, it is necessary to confirm their safety with other toxicity tests using eukaryotic cell lines. Generally, other authors also reported that apatite-based compounds are not hemolytic. Apart from the hemolysis assays, they also performed tests like morphology observation of platelets and measurement of blood clotting time. Each of them confirmed that pure hydroxyapatite is safe in this respect.[56]

4. CONCLUSIONS

The aim of this study was to investigate the structural and antibacterial activity of silver-doped hydroxyapatite and fluorapatite. The successful incorporation of silver ions into the obtained matrix was confirmed by X-ray diffraction and the EDS technique. The SEM and TEM images were recorded to confirm the nanometric size of the obtained materials. The typical active vibrational bands were ascribed to the apatite structure in the infrared spectrum. The studied hydroxy- and fluorapatites doped with 1.0, 2.5, and 5.0 mol % Ag^+ have demonstrated the antibacterial activity, especially against Gram-negative species. In the present research, comparison of the antimicrobial activity between hydroxy- and fluorapatites was not possible because of the uneven silver content between corresponding samples. All materials have inhibited the growth of *P. aeruginosa*, preventing biofilm formation on the pellets' surface. The nanopowder and PTFE composition have

https://dx.doi.org/10.1021/acsomega.0c03044
ACS Omega 2020, 5, 24546−24557

decreased the ability to prevent bacterial growth, but the hydrophobic surface of the PTFE has played the antibiofilm role. All materials might be considered safe because of a lack of hemolysis. The apatite might be considered as a promising bone- or teeth-filling material after studies of their biocompatibility and toxicity.

■ ASSOCIATED CONTENT

Supporting Information

The Supporting Information is available free of charge at https://pubs.acs.org/doi/10.1021/acsomega.0c03044.

Representative pellets of 5.0 mol % Ag^+:HAp, (b) 5.0 mol % Ag^+:FAp, and tetrafluoroethylene with 10.0 wt % of hydroxyapatite (PTFE@Ag^+:10HAp) and 10.0 wt % of fluorapatite (PTFE@Ag^+:10FAp) composites (Figure S1); view of the unit cell of fluorapatite crystal along [001] and coordination polyhedron of Ca^{2+} cations in the crystal structure of the fluorapatite (Figure S2); X-ray diffraction correlation of 2.5 mol % Ag^+:FAp with hydroxyapatite and fluorapatite (Figure S3); particle size distribution of poly(tetrafluoroethylene) PTFE dispersed in deionized water (Figure S4); Ag^+ release from tetrafluoroethylene composites with 10.0 wt % hydroxyapatite and 10 wt % fluorapatite (Figure S5); hemolysis caused by HAp/FAp doped with 1.0, 2.5, and 5.0 mol% Ag^+ compared to hemolysis caused by 1% SDS (mean ± SD, n = 3; all results were statistically significant ($p < 0.05$) (Figure S6) (PDF)

■ AUTHOR INFORMATION

Corresponding Author

Rafal J. Wiglusz − *Institute of Low Temperature and Structure Research, Polish Academy of Sciences, 50-422 Wroclaw, Poland*; orcid.org/0000-0001-8458-1532; Phone: +48(071)3954159; Email: r.wiglusz@intibs.pl; Fax: +48(071)3441029

Authors

Sara Targonska − *Institute of Low Temperature and Structure Research, Polish Academy of Sciences, 50-422 Wroclaw, Poland*

Justyna Rewak-Soroczynska − *Institute of Low Temperature and Structure Research, Polish Academy of Sciences, 50-422 Wroclaw, Poland*

Agata Piecuch − *Institute of Genetics and Microbiology, University of Wroclaw, 51-148 Wroclaw, Poland*

Emil Paluch − *Department of Microbiology, Faculty of Medicine, Wroclaw Medical University, 50-376 Wroclaw, Poland*

Damian Szymanski − *Institute of Low Temperature and Structure Research, Polish Academy of Sciences, 50-422 Wroclaw, Poland*

Complete contact information is available at: https://pubs.acs.org/10.1021/acsomega.0c03044

Notes

The authors declare no competing financial interest.

■ ACKNOWLEDGMENTS

The authors are grateful to the National Science Centre for the financial support in the course of realization of the Projects "Preparation and characterization of biocomposites based on nanoapatites for theranostics" (no. UMO-2015/19/B/ST5/01330) and "Elaboration and characteristics of biocomposites with anti-virulent and anti-bacterial properties against *P. aeruginosa*" (no. UMO-2016/21/B/NZ6/01157). They thank E. Bukowski for performing XRD measurements, L. Grosman for AAS measurements, Prof. Z. Drulis-Kawa for sharing bacterial strains, and M. Małecka for TEM measurements.

■ REFERENCES

(1) Sudarsanan, K.; Young, R. A. Significant Precision in Crystal Structural Details. Holly Springs Hydroxyapatite. *Acta Crystallogr., Sect. B: Struct. Crystallogr. Cryst. Chem.* **1969**, *25*, 1534−1543.

(2) Tite, T.; Popa, A. C.; Balescu, L. M.; Bogdan, I. M.; Pasuk, I.; Ferreira, J. M. F.; Stan, G. E. Cationic Substitutions in Hydroxyapatite: Current Status of the Derived Biofunctional Effects and Their in Vitro Interrogation Methods. *Materials* **2018**, *11*, No. 2081.

(3) Mucalo, M. *Hydroxyapatite (HAp) for Biomedical Applications*; Woodhead Publishing: Amsterdam, 2015.

(4) Kolmas, J.; Groszyk, E.; Kwiatkowska-Różycka, D. Substituted Hydroxyapatites with Antibacterial Properties. *BioMed Res. Int.* **2014**, *2014*, 1−15.

(5) Nasrollahzadeh, M.; Zahraei, A.; Pourbasheer, E. Catalytic Activity and Antibacterial Properties of Nanopolymer-Supported Copper Complex for C-N Coupling Reactions of Amines and Nitrogen-Containing Heterocycles with Aryl Halides. *Monatsh. Chem.* **2015**, *146*, 1329−1334.

(6) Tsai, S. W.; Yu, W. X.; Hwang, P. A.; Huang, S. S.; Lin, H. M.; Hsu, Y. W.; Hsu, F. Y. Fabrication and Characterization of Strontium-Substituted Hydroxyapatite-CaO-$CaCO_3$ Nanofibers with a Mesoporous Structure as Drug Delivery Carriers. *Pharmaceutics* **2018**, *10*, No. 179.

(7) Pal, S.; Tak, Y. K.; Song, J. M. Does the Antibacterial Activity of Silver Nanoparticles Depend on the Shape of the Nanoparticle? A Study of the Gram-Negative Bacterium *Escherichia coli*. *Appl. Environ. Microbiol.* **2007**, *73*, 1712−1720.

(8) Lemire, J. A.; Harrison, J. J.; Turner, R. J. Antimicrobial Activity of Metals: Mechanisms, Molecular Targets and Applications. *Nat. Rev. Microbiol.* **2013**, *11*, 371−384.

(9) Hajipour, M. J.; Fromm, K. M.; Akbar Ashkarran, A.; Jimenez de Aberasturi, D.; de Larramendi, I. R.; Rojo, T.; Serpooshan, V.; Parak, W. J.; Mahmoudi, M. Antibacterial Properties of Nanoparticles. *Trends Biotechnol.* **2012**, 499−511.

(10) Kim, J. S.; Kuk, E.; Yu, K. N.; Kim, J. H.; Park, S. J.; Lee, H. J.; Kim, S. H.; Park, Y. K.; Park, Y. H.; Hwang, C. Y.; Kim, Y. K.; Lee, Y. S.; Jeong, D. H.; Cho, M. H. Antimicrobial Effects of Silver Nanoparticles. *Nanomedicine* **2007**, *3*, 95−101.

(11) Morones, J. R.; Elechiguerra, J. L.; Camacho, A.; Holt, K.; Kouri, J. B.; Ramírez, J. T.; Yacaman, M. J. The Bactericidal Effect of Silver Nanoparticles. *Nanotechnology* **2005**, *16*, 2346−2353.

(12) Sondi, I.; Salopek-Sondi, B. Silver Nanoparticles as Antimicrobial Agent: A Case Study on *E. coli* as a Model for Gram-Negative Bacteria. *J. Colloid Interface Sci.* **2004**, *275*, 177−182.

(13) Lara, H. H.; Garza-Treviño, E. N.; Ixtepan-Turrent, L.; Singh, D. K. Silver Nanoparticles Are Broad-Spectrum Bactericidal and Virucidal Compounds. *J. Nanobiotechnol.* **2011**, No. 30.

(14) Klasen, H. J. Historical Review of the Use of Silver in the Treatment of Burns. I. Early uses. *Burns* **2000**, 117−130.

(15) Ciobanu, C. S.; Iconaru, S. L.; Le Coustumer, P.; Constantin, L. V.; Predoi, D. Antibacterial Activity of Silver-Doped Hydroxyapatite Nanoparticles against Gram-Positive and Gram-Negative Bacteria. *Nanoscale Res. Lett.* **2012**, *7*, No. 324.

(16) Ciobanu, C. S.; Iconaru, S. L.; Chifiriuc, M. C.; Costescu, A.; Le Coustumer, P.; Predoi, D. Synthesis and Antimicrobial Activity of Silver-Doped Hydroxyapatite Nanoparticles. *BioMed Res. Int.* **2013**, *2013*, No. 916218.

(17) Dubnika, A.; Loca, D.; Rudovica, V.; Parekh, M. B.; Berzina-Cimdina, L. Functionalized Silver Doped Hydroxyapatite Scaffolds for Controlled Simultaneous Silver Ion and Drug Delivery. *Ceram. Int.* **2017**, *43*, 3698−3705.

(18) Olsen, I. Biofilm-Specific Antibiotic Tolerance and Resistance. *Eur. J. Clin. Microbiol. Infect. Dis.* **2015**, 877−886.
(19) Allaker, R. P. Critical Review in Oral Biology & Medicine: The Use of Nanoparticles to Control Oral Biofilm Formation. *J. Dent. Res.* **2010**, *89*, 1175−1186.
(20) Zhao, L.; Chu, P. K.; Zhang, Y.; Wu, Z. Antibacterial Coatings on Titanium Implants. *J. Biomed. Mater. Res., Part B* **2009**, 470−480.
(21) Dunne, W. M. Bacterial Adhesion: Seen Any Good Biofilms Lately? *Clin. Microbiol. Rev.* **2002**, 155−166.
(22) Nasrollahzadeh, M.; Motahharifar, N.; Ghorbannezhad, F.; Soheili Bidgoli, N. S.; Baran, T.; Varma, R. S. Recent Advances in Polymer Supported Palladium Complexes as (Nano)Catalysts for Sonogashira Coupling Reaction. *Mol. Catal.* **2020**, *480*, No. 110645.
(23) Nasrollahzadeh, M.; Sajjadi, M.; Shokouhimehr, M.; Varma, R. S. Recent Developments in Palladium (Nano)Catalysts Supported on Polymers for Selective and Sustainable Oxidation Processes. *Coord. Chem. Rev.* **2019**, *397*, 54−75.
(24) Guan, R.-G.; Johnson, I.; Cui, T.; Zhao, T.; Zhao, Z.-Y.; Li, X.; Liu, H. Electrodeposition of Hydroxyapatite Coating on Mg-4.0Zn-1.0Ca-0.6Zr Alloy and in Vitro Evaluation of Degradation, Hemolysis, and Cytotoxicity. *J. Biomed. Mater. Res., Part A* **2012**, *100A*, 999−1015.
(25) Targonska, S.; Szyszka, K.; Rewak-Soroczynska, J.; Wiglusz, R. J. A New Approach to Spectroscopic and Structural Studies of the Nano-Sized Silicate-Substituted Hydroxyapatite Doped with Eu^{3+} Ions. *Dalton Trans.* **2019**, *48*, 8303−8316.
(26) Sobierajska, P.; Wiglusz, R. J. Influence of Li^{+} Ions on the Physicochemical Properties of Nanocrystalline Calcium−Strontium Hydroxyapatite Doped with Eu^{3+} Ions. *New J. Chem.* **2019**, *43*, 14908−14916.
(27) Wei, M.; Evans, J.; Bostrom, T.; Grondahl, L. Synthesis and Characterization of Hydroxyapatite, Fluoride-Substituted Hydroxyapatite and Fluorapatite. *J. Mater. Sci.: Mater. Med.* **2003**, *14*, 311−320.
(28) Newbury, D. E.; Ritchie, N. W. M. Performing Elemental Microanalysis with High Accuracy and High Precision by Scanning Electron Microscopy/Silicon Drift Detector Energy-Dispersive X-Ray Spectrometry (SEM/SDD-EDS). *J. Mater. Sci.* **2015**, 493−518.
(29) Ma, G.; Liu, X. Y. Hydroxyapatite: Hexagonal or Monoclinic? *Cryst. Growth Des.* **2009**, *9*, 2991−2994.
(30) Shannon, R. D. Revised Effective Ionic Radii and Systematic Studies of Interatomic Distances in Halides and Chalcogenides. *Acta Crystallogr., Sect. A: Found. Adv.* **1976**, *32*, 751−767.
(31) Sudarsanan, K.; Mackie, P. E.; Young, R. A. Comparison of Synthetic and Mineral Fluorapatite, Ca5 (PO4)3F, in Crystallographic Detail. *Mater. Res. Bull.* **1972**, *7*, 1331−1337.
(32) Fleet, M. E.; Liu, X.; Pan, Y. Site Preference of Rare Earth Elements in Hydroxyapatite [Ca10(PO4)6(OH)2]. *J. Solid State Chem.* **2000**, *149*, 391−398.
(33) Zawisza, K.; Wiglusz, R. J. Preferential Site Occupancy of Eu^{3+} Ions in Strontium Hydroxyapatite Nanocrystalline − $Sr_{10}(PO_4)_6(OH)_2$ − Structural and Spectroscopic Characterisation. *Dalton Trans.* **2017**, *46*, 3265−3275.
(34) Stanić, V.; Radosavljević-Mihajlović, A. S.; Živković-Radovanović, V.; Nastasijević, B.; Marinović-Cincović, M.; Marković, J. P.; Budimir, M. D. Synthesis, Structural Characterisation and Antibacterial Activity of Ag+-Doped Fluorapatite Nanomaterials Prepared by Neutralization Method. *Appl. Surf. Sci.* **2015**, *337*, 72−80.
(35) Rietveld, H. M. A Profile Refinement Method for Nuclear and Magnetic Structures. *J. Appl. Crystallogr.* **1969**, *2*, 65−71.
(36) Lutterotti, L.; Matthies, S.; Wenk, H.-R. *MAUD: A Friendly Java Program for Material Analysis Using Diffraction*, Newsletter No. 21; International Union of Crystallography, 1999; Vol. *21*, pp 14−15.
(37) Qu, H.; Wei, M. Synthesis and Characterization of Fluorine-Containing Hydroxyapatite by a PH-Cycling Method. *J. Mater. Sci.: Mater. Med.* **2005**, *16*, 129−133.
(38) Feng, B.; Fang, X.; Wang, H.-X.; Dong, W.; Li, Y.-C. The Effect of Crystallinity on Compressive Properties of Al-PTFE. *Polymers* **2016**, *8*, No. 356.
(39) Kang, W.; Li, F.; Zhao, Y.; Qiao, C.; Ju, J.; Cheng, B. Fabrication of Porous Fe2O3/PTFE Nanofiber Membranes and Their Application as a Catalyst for Dye Degradation. *RSC Adv.* **2016**, *6*, 32646−32652.
(40) Sobierajska, P.; Pazik, R.; Zawisza, K.; Renaudin, G.; Nedelec, J. M.; Wiglusz, R. J. Effect of Lithium Substitution on the Charge Compensation, Structural and Luminescence Properties of Nanocrystalline Ca10(PO4)6F2 Activated with Eu^{3+} Ions. *CrystEngComm* **2016**, *18*, 3447−3455.
(41) Marycz, K.; Sobierajska, P.; Smieszek, A.; Maredziak, M.; Wiglusz, K.; Wiglusz, R. J. Li+ Activated Nanohydroxyapatite Doped with Eu^{3+} Ions Enhances Proliferative Activity and Viability of Human Stem Progenitor Cells of Adipose Tissue and Olfactory Ensheathing Cells. Further Perspective of NHAP:Li^{+}, Eu^{3+} Application in Theranostics. *Mater. Sci. Eng., C* **2017**, *78*, 151−162.
(42) Balan, E.; Delattre, S.; Roche, D.; Segalen, L.; Morin, G.; Guillaumet, M.; Blanchard, M.; Lazzeri, M.; Brouder, C.; Salje, E. K. H. Line-Broadening Effects in the Powder Infrared Spectrum of Apatite. *Phys. Chem. Miner.* **2011**, *38*, 111−122.
(43) Tredwin, C. J.; Georgiou, G.; Kim, H. W.; Knowles, J. C. Hydroxyapatite, Fluor-Hydroxyapatite and Fluorapatite Produced via the Sol-Gel Method: Bonding to Titanium and Scanning Electron Microscopy. *Dent. Mater.* **2013**, *29*, 521−529.
(44) Baumer, A.; Ganteaume, M.; Klee, W. E. Determination of OH^{-} Ions in Hydroxyfluorapatites by Infrared Spectroscopy. *Bull. Minéral.* **1985**, *108*, 145−152.
(45) Bhullar, S. K.; Bedeloglu, A.; Jun, M. B. G. Characterization and Auxetic Effect of Polytetrafluoroethylene Tubular Structure. *Int. J. Adv. Sci. Eng.* **2014**, *1*, 8−13.
(46) Wang, H.; Wen, Y.; Peng, H.; Zheng, C.; Li, Y.; Wang, S.; Sun, S.; Xie, X.; Zhou, X. Grafting Polytetrafluoroethylene Micropowder via in Situ Electron Beam Irradiation-Induced Polymerization. *Polymers* **2018**, *10*, No. 503.
(47) Martínez-Sanmiguel, J. J.; Zarate-Triviño, D. G.; Hernandez-Delgadillo, R.; Giraldo-Betancur, A. L.; Pineda-Aguilar, N.; Galindo-Rodríguez, S. A.; Franco-Molina, M. A.; Hernández-Martínez, S. P.; Rodríguez-Padilla, C. Anti-Inflammatory and Antimicrobial Activity of Bioactive Hydroxyapatite/Silver Nanocomposites. *J. Biomater. Appl.* **2019**, *33*, 1314−1326.
(48) Dakal, T. C.; Kumar, A.; Majumdar, R. S.; Yadav, V. Mechanistic Basis of Antimicrobial Actions of Silver Nanoparticles. *Front. Microbiol.* **2016**, *7*, No. 1831.
(49) Fielding, G. A.; Roy, M.; Bandyopadhyay, A.; Bose, S. Antibacterial and Biological Characteristics of Silver Containing and Strontium Doped Plasma Sprayed Hydroxyapatite Coatings. *Acta Biomater.* **2012**, *8*, 3144−3152.
(50) Sodagar, A.; Akhavan, A.; Hashemi, E.; Arab, S.; Pourhajibagher, M.; Sodagar, K.; Kharrazifard, M. J.; Bahador, A. Evaluation of the Antibacterial Activity of a Conventional Orthodontic Composite Containing Silver/Hydroxyapatite Nanoparticles. *Prog. Orthod.* **2016**, *17*, No. 40.
(51) Besinis, A.; Hadi, S. D.; Le, H. R.; Tredwin, C.; Handy, R. D. Antibacterial Activity and Biofilm Inhibition by Surface Modified Titanium Alloy Medical Implants Following Application of Silver, Titanium Dioxide and Hydroxyapatite Nanocoatings. *Nanotoxicology* **2017**, *11*, 327−338.
(52) Zhao, L.; Ashraf, M. A. Influence of Silver-Hydroxyapatite Nanocomposite Coating on Biofilm Formation of Joint Prosthesis and Its Mechanism. *West Indian Med. J.* **2015**, *64*, 506−513.
(53) Riau, A. K.; Aung, T. T.; Setiawan, M.; Yang, L.; Yam, G. H. F.; Beuerman, R. W.; Venkatraman, S. S.; Mehta, J. S. Surface Immobilization of Nano-Silver on Polymeric Medical Devices to Prevent Bacterial Biofilm Formation. *Pathogens* **2019**, *8*, No. 93.
(54) Porrelli, D.; Travan, A.; Turco, G.; Crosera, M.; Borgogna, M.; Donati, I.; Paoletti, S.; Adami, G.; Marsich, E. Antibacterial-Nanocomposite Bone Filler Based on Silver Nanoparticles and Polysaccharides. *J. Tissue Eng. Regener. Med.* **2018**, *12*, e747−e759.
(55) Aditya, N. P.; Chimote, G.; Gunalan, K.; Banerjee, R.; Patankar, S.; Madhusudhan, B. Curcuminoids-Loaded Liposomes in Combina-

https://dx.doi.org/10.1021/acsomega.0c03044
ACS Omega 2020, 5, 24546−24557

tion with Arteether Protects against *Plasmodium berghei* Infection in Mice. *Exp. Parasitol.* **2012**, *131*, 292−299.
(56) Ooi, C.-H.; Ling, Y. P.; Abdullah, W. Z.; Mustafa, A. Z.; Pung, S.-Y.; Yeoh, F.-Y. Physicochemical Evaluation and in Vitro Hemocompatibility Study on Nanoporous Hydroxyapatite. *J. Mater. Sci.: Mater. Med.* **2019**, *30*, No. 44.

https://dx.doi.org/10.1021/acsomega.0c03044
ACS Omega 2020, 5, 24546−24557